22. International winter meeting on nuclear physics
Bormio (Italy) 23-27 Jan 1984
CEA-CONF--7168

Rapport DPh.N-Saclay n° 2120 - 01/1984

HEAVY ION ELASTIC SCATTERINGS

Michel C. Mermaz

Service de Physique Nucléaire - Basse Energie
CEN Saclay, 91191 Gif-sur-Yvette Cedex, France

HEAVY ION ELASTIC SCATTERINGS

Michel C. Mermaz

Service de Physique Nucléaire - Basse Energie
CEN Saclay, 91191 Gif-sur-Yvette Cedex, France

Abstract : A general theoretical and experimental review of diffractive and refractive phenomena will be presented. Semi-classical considerations will be discussed in connection with optical predictions.

1. Introduction

Diffraction and refraction play an important role in particle elastic scattering and in the past the two aspects of this phenomenon have led to many confusing discussions since two much light was some time put only in one aspects of the mechanism[1]). Of course the optical model treats correctly and simultaneously both phenomena but without disentangling them. Semi-classical discussions in terms of trajectories emphasize the refractive aspect due to the real part of the optical potential. In a second stage, the separation due to to R.C. Fuller of the quantal cross section into two components coming from opposite side of the target nucleus allows to understand better the refractive phenomenon and the origin of the observed oscillations in the elastic scattering angular distributions[2]). Furthermore, we shall see that the real part of the potential is responsible of a Coulomb and a nuclear rainbow which allows to determine better the nuclear potential in the interior region near the nuclear surface since the volume absorption eliminates any effect of the real part of the potential for the internal partial scattering waves. Resonance phenomena seen in heavy ion scattering will be discussed in terms of optical model potential and Regge pole analysis. Compound nucleus resonances or quasi-molecular states can be indeed the more correct and fundamental alternative.

2. Schematic description of the elastic scattering

In fig.1 is presented a typical particle real potential including its Coulomb barrier. Just below has been drawn the WKB deflection function corresponding to an energy higher than the Coulomb barrier height[3]). At each impact parameter, b, corresponds a deflection angle, θ_b ; for large b, we are dealing with Rutherford trajectories. The large parameter values of the deflection function correspond to trajectories named NEAR in the bottom part of the figure where scattered trajectories are drawn. They are called near trajectories because they are the closest ones to the detector but their colliding distances are large. The negative part of the deflection function, θ_b, corresponds to FAR trajectories and are close to the nucleus center but far from the detector. A pole ($\theta_{b_p} = -\infty$) can occur in the deflection function. It means that we are dealing with a permanent orbiting of the projectile around the target nucleus. The condition of the presence

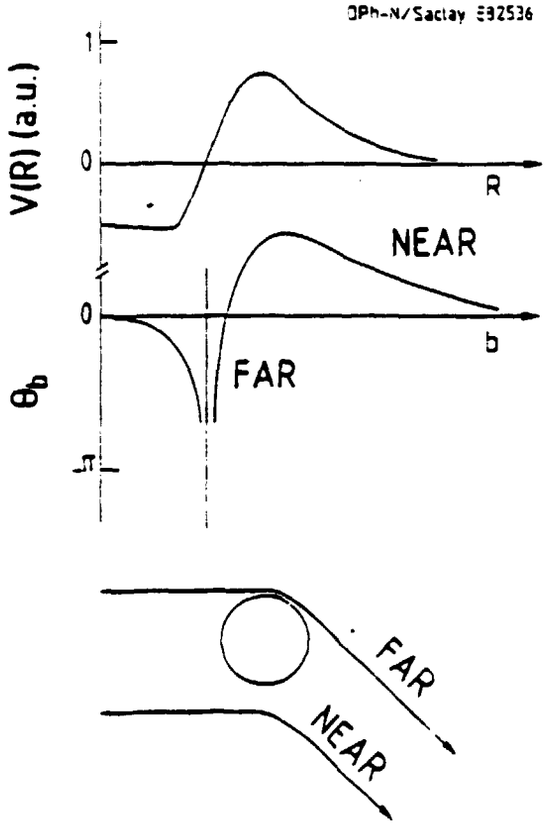

Fig. 1. Schematic elastic scattering graphs : Coulomb plus nuclear potential real part only, with its corresponding deflection function, WKB calculations and far-side, near-side trajectories for a same detection angle. The center of mass energy is higher than the Coulomb barrier.

of a pole has been stated by W.H. Miller[4]) : the orbiting occurs for all center-of-mass energies smaller than the following quantity.

$$E_{orb.} = \left[V(r) + \frac{r}{2}\,\frac{d}{dr}\,V(r)\right]_{max} \qquad (1)$$

Above this energy we have only a nuclear rainbow which means that there is no trajectory more backward than this value $|\theta_{N.R.}| < \pi$. In the same way as soon as the center of mass energy is higher than the height of the Coulomb barrier there is no more trajectory for the near side more backward than the Coulomb rainbow $\theta_{C.R.} < \pi$.

The presence of absorption will wash out these pictures especially for the action of the inner part of the real potential. It had been noticed in the past that the presence of strong absorption leads to the continuous Igo ambiguity[5]) on the determination of the real and imaginary part of the potential. Thus the elastic scattering is only sensitive to the tail of the nuclear potential. In this latter case only one point is defined for the potential, there exists a large ambiguity in the slope of the potential at this point ; we know only V(R) and W(R) at $R \simeq 1.55\ (A_T^{1/3} + A_p^{1/3})$ fm below

let us say, 10 MeV/A_p incident energy[6,7]). This is the sensitive radius and also the radius of the quater point, half absorption and Coulomb barrier.

The elastic scattering amplitude for charged particle is given by the usual following formula :

$$f(\theta) = f_{Coul}(\theta) + \frac{i}{2k} \sum_{\ell=0}^{\infty} (2\ell+1)\, e^{2i\sigma_\ell} (1 - |S_\ell| e^{2i\delta_\ell})\, P_\ell(\cos\theta) \qquad (2)$$

with the obvious notations. The cross section is therefore

$$\sigma(\theta) = |f(\theta)|^2 \qquad (3)$$

From a semi classical analogy an optical model deflection function can be built :

$$\theta_\ell = 2 \frac{d\sigma_\ell}{d\ell} + 2 \frac{d\delta_\ell}{d\ell} \qquad (4)$$

leading to the following formula we shall use in this paper :

$$\theta_\ell = 2 \arctan \frac{\eta}{\ell} + 2\left(\delta_{\ell+1} - \delta_\ell\right) \qquad (5)$$

Let us remark that the WKB deflection function for a Coulomb plus nuclear potential is always different from the optical model one especially for small angular momentum ℓ as soon as the center of mass energy is higher than the top of the Coulomb barrier.

We shall see that the shape of the angular distribution depends only on the two following ingredients : the modulus of the S matrix $|S_\ell|$ and the deflection function θ_ℓ, see formula (5).

The amplitude cross section for the nuclear part has been decomposed by R.C. Fuller[2]) in the following way :

$$f(\theta) = f_{FAR}^{Coul}(\theta) + f_{NEAR}^{Coul}(\theta) + f_{FAR}^{(+)}(\theta) + f_{NEAR}^{(-)}(\theta) \qquad (6)$$

with, for the nuclear part :

$$\begin{aligned} f_{FAR}^{(+)}(\theta) &= \frac{i}{2k} \sum_{\ell=0}^{\infty} (2\ell+1)\, e^{2i\sigma_\ell} (S_\ell - 1)\, \tilde{Q}_\ell^{+}(\cos\theta) \\ f_{NEAR}^{(-)}(\theta) &= \frac{i}{2k} \sum_{\ell=0}^{\infty} (2\ell+1)\, e^{2i\sigma_\ell} (S_\ell - 1)\, \tilde{Q}_\ell^{-}(\cos\theta) \end{aligned} \qquad (7)$$

where

$$P_\ell(\cos\theta) = \tilde{Q}_\ell^+(\cos\theta) + \tilde{Q}_\ell^-(\cos\theta) \qquad (8)$$

The $\tilde{Q}_\ell^\pm$ are linear combination of one Legendre polynomial with one polynomial of the second kind. (See Appendix A).

The Coulomb amplitude, $f_{Coul}(\theta)$, which does not admit a usable partial wave expansion, has been also analytically split in a near side and a far side contribution. We know that the matrix elements $|S_\ell|e^{2i\delta_\ell}$ can be determined by either a phase shift analysis or an optical model analysis of the experimental data. Then it is possible to calculate cross sections for the near- and far-trajectories on both sides of the nucleus. We shall see later on, with this technics that it is possible to understand better the behaviour of the differential cross section and to probe better the interior of the nuclear potential near the surface.

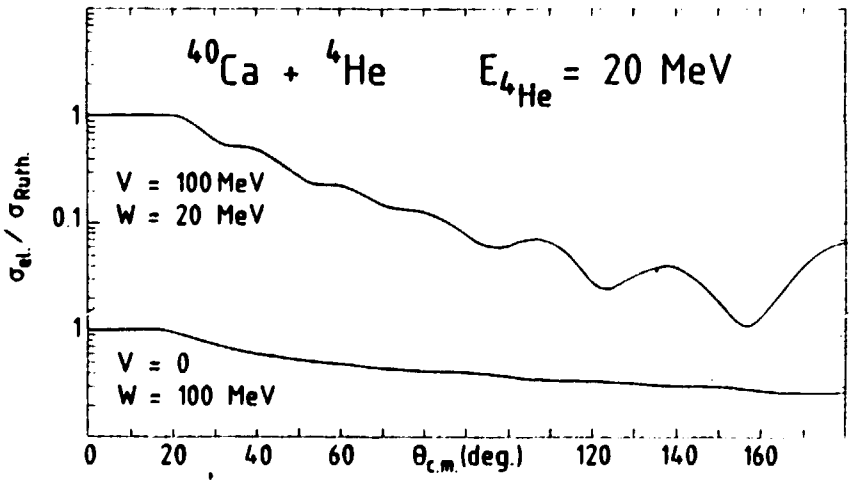

Fig. 2. Calculated angular distributions for the α-particle elastic scattering on ^{40}Ca target nucleus for two extreme cases of optical potential : diffraction and refraction.

In fig. 2 are presented two extreme cases of α-particle scattering in the vicinity of Coulomb barrier, for didactic reasons. The diffractional case corresponds to an imaginary depth W = 100 MeV for a real nuclear potential V = 0. At forward angle, the angular distribution is purely Rutherford, the decrease of the cross section at backward angle is due to strong absorption of the Coulomb trajectories intercepted by the target nucleus. Such behaviour is called a Fresnel pattern. In the same figure, the other extreme case is mainly refractive since the imaginary depth W is small, 20 MeV, with respect to the real part 100 MeV. Strong oscillations are now present at backward angles. This can be immediately understood by

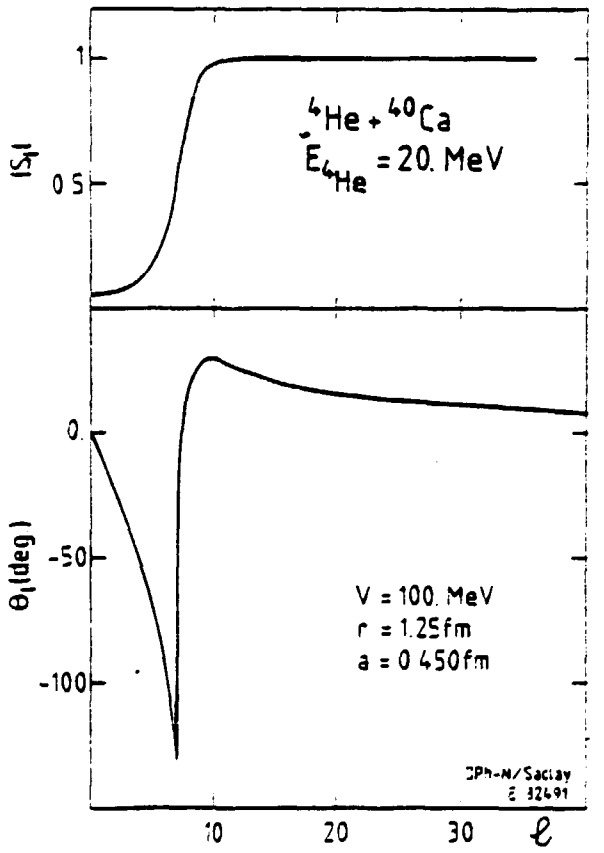

Fig. 3. The modulus of the optical model S-matrix along with the WKB total deflection function. The deflection function plays a role in the elastic scattering only when the modulus of the scattering matrix S is different from zero.

looking at fig. 3 where the deflection function of this case is drawn along with the modulus of the S-matrix. We can see that there is a strong discontinuity in the WKB deflection function just below the grazing wave angular momentum : $|S_{\ell_g}| = 0.50$. Consequently the Legendre polynomials in the elastic scattering amplitude formula (2) do not add up gently any more, and oscillations are then generated by the approximate periodicity $\Delta\theta = 180°/\ell_g$ We have plotted the WKB deflection function instead of the optical model one, formula (5), since the grazing wave, ℓ_g, is to small. More light can be gained about this oscillatory pattern by looking at the behaviour of the near-side and far-side components of the elastic cross sections. At forward angle, in fig. 4, the far-side component is small but at backward angle the two components are comparable and consequently they interfere and produce the oscillations observed in the total elastic cross section of fig. 2. The periodicity in the far-side component is due to the beating of two waves in the deflection function located on both sides of the deep negative minima, see fig. 3. The periodicity is $180°/|\ell_> - \ell_<|$. [ref.[2])].

The case of fig. 2 was corresponding to an orbiting phenomenon since the condition of W.H. Miller[4]) for this process is fulfilled, see formula (1) Now we consider the case of a nuclear rainbow for which the center of mass energy is much greater than the value of equation(1). The result is displayed

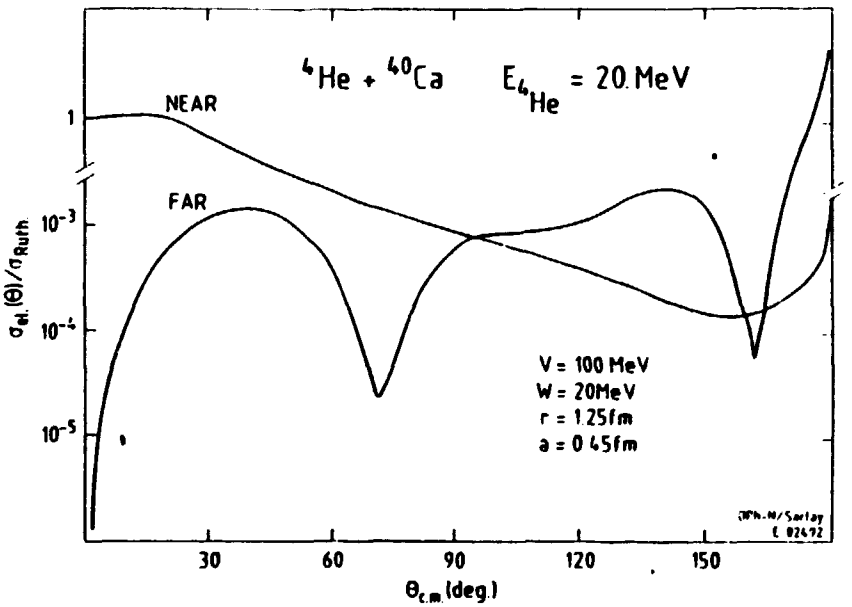

Fig. 4. The far-side and near-side decomposition of the elastic scattering cross section due to the R.C. Fuller formalism. In order to understand interference effect between far- and near-trajectories, it is very important to take care of the change of scale for the two curves.

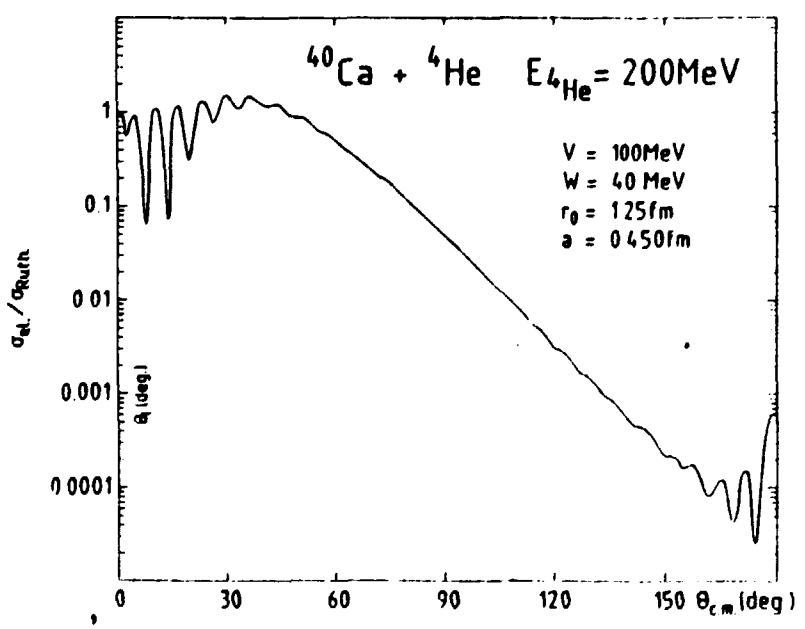

Fig. 5. Calculated angular distribution of the α-particle elastic scattering on ^{40}Ca target nucleus. The forward angle general pattern is a strong signature of a presence of a nuclear rainbow, please notice the reminescent oscillations at very backward angles. The computation was run with a very high accuracy : code ECIS of J. Raynal

in fig. 5 and is rather typical. It is possible to see in fig. 6 the optical model deflection function along with the S-matrix element curve ; the nuclear rainbow is about 75° for a grazing angular momentum of ℓ_g = 24.

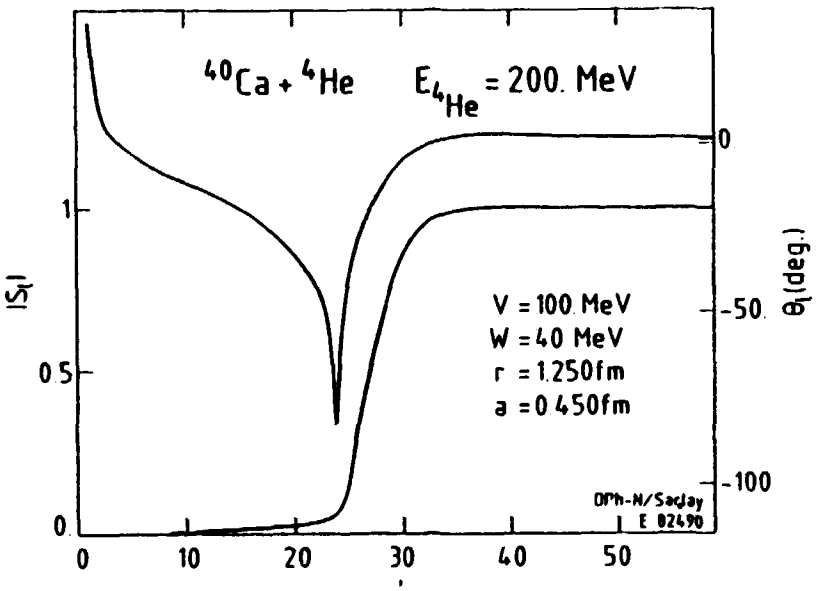

Fig. 6. Modulus of the optical model elastic scattering S along with the optical model deflection function. Herein again the deflection function contributes to the behaviour of the angular distribution only for S-matrix element values different from zero

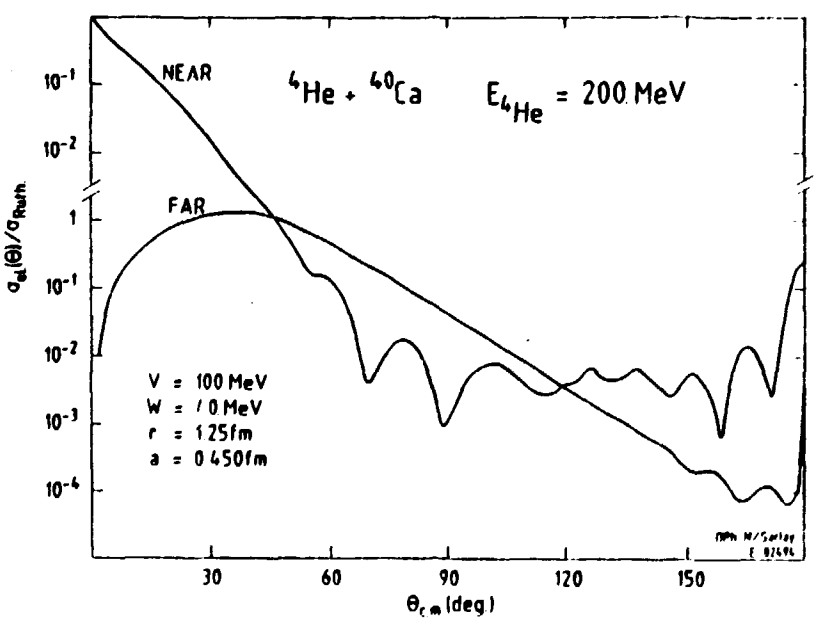

Fig. 7. The far-side and near-side decomposition of the 200 MeV α-particle elastic scattering on ^{40}Ca target nucleus. Please note, the importance change of scale between the two curves

The elastic angular distribution presents oscillation of $180°/\ell_g$ periodicity at forward angle of this nuclear rainbow value. Similar oscillations can also be seen at very backward angles. On the one hand the far-side and near-side separation of the cross section explains clearly the origin of the oscillations at forward angles, see figure 7 where the two contributions are equivalent and consequently interfere ; on the other hand at backward angles the structureless far-side component dominates. Please note the change of scale for the two curves on fig. 7. At very backward angles the far-side and near-side components are again of the same order of magnitude ; in this way, they reproduce, by interference, an oscillatory pattern in the total cross section of fig. 5.

4. ELASTIC SCATTERING EXPERIMENTAL RESULTS.

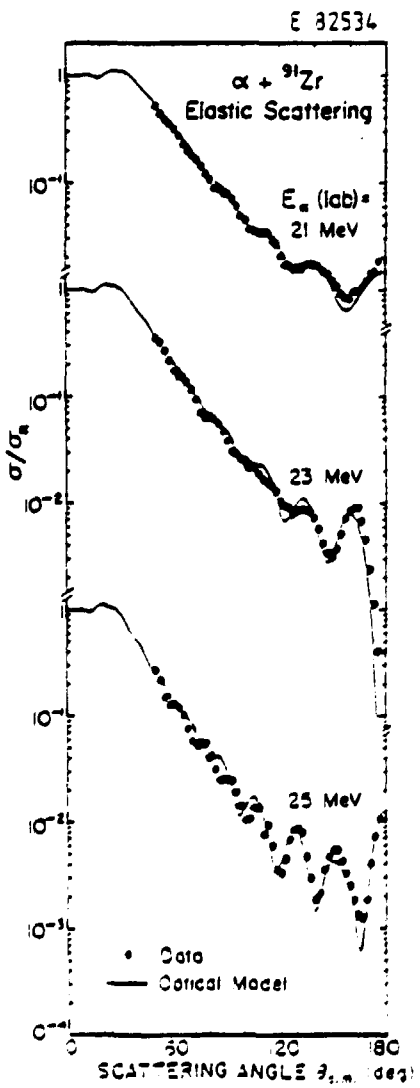

Fig. 8. Angular distribution of the α-particle elastic scattering on ^{91}Zr target nucleus. Evidence of clean signature of orbiting phenomena, see ref.[8]).

α-particle elastic scatterings on ^{89}Y and $^{90,91,94}Zr$ target nuclei show clearly evidence for orbiting phenomena in the range of 18- to 26-MeV incident energy[8]). Several angular distributions for this set of targets are reproduced by the following unique 4-parameter potential :

$$U_{opt}(r) = -(V+iW)/\{1+\exp[(r-R)/a]\} \qquad (9)$$

with V = 200 MeV, W = 25.2 MeV and $R = 1.37\ A^{1/3}$fm. and a = 0.56 fm.

The classical condition of W.H. Miller[4]) for orbiting, is fulfilled by the real part of this potential. The value of imaginary depth is small in front of the real-part value, then the potential is transparent enough for the grazing wave orbital numbers which produce the oscillatory pattern. The authors at that time, eight years ago, have not tried to locate the sensitive region of

the potential which allows to reproduce the experimental data. The figure 8 presents a typical result of orbiting phenomena for alpha scattering on ^{91}Zr target nucleus. At 23 MeV incident energy, the grazing wave is extremely near a pole in the deflection function since a deep minimum is seen at 180° in the angular distribution which means that the α-particle is catched by the target nucleus. If a given potential produce orbiting at low incident energy, at higher energy nuclear rainbow phenomenon has to be evidenced. This is indeed the case as it can be viewed for α-particle scattering on several target nuclei on fig. 9, the incident energy is 140 MeV [ref.[9]].

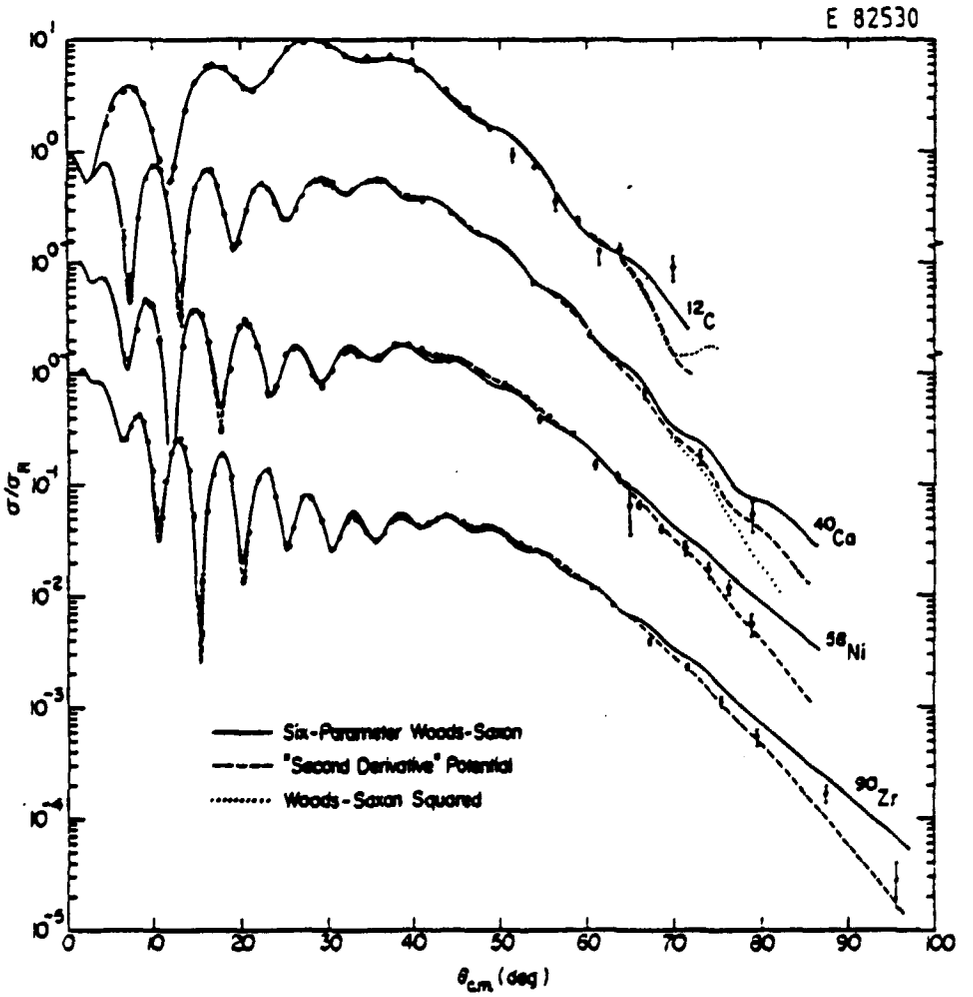

Fig. 9. Angular distributions of α-particle elastic scattering on various target nuclei. The shapes are signatures of rainbow phenomena. The curves are optical model fits, see ref.[9]).

The curves of fig. 9 were produced by an optical model analysis and have to be compared with the expected curve of fig. 5, the same area of physics. Data which display orbiting phenomenon or nuclear rainbow give better determination of the optical potential than those which display only diffraction phenomena (strong absorption). We shall come back later on this point.

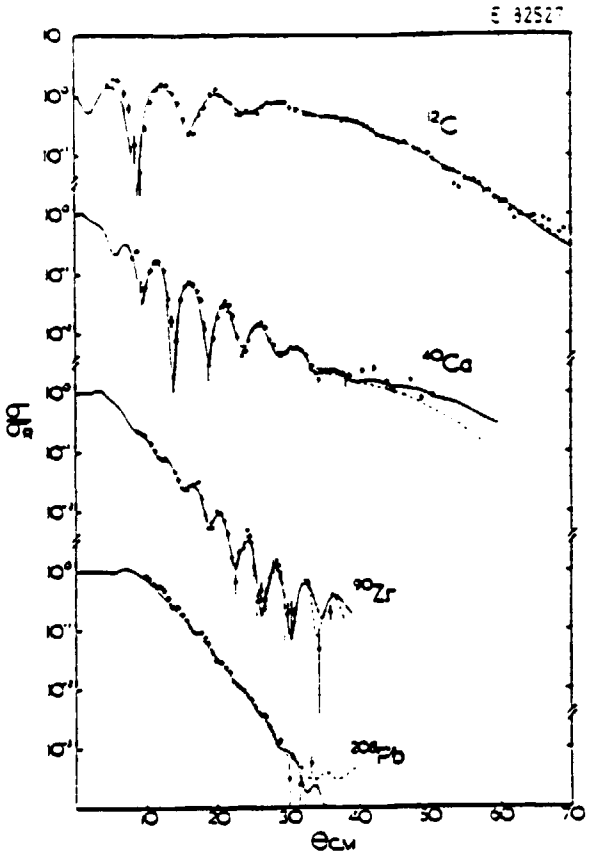

Fig. 10. Angular distributions of the ^{6}Li particle scattering on various target nuclei. Clean nuclear rainbow signatures can be seen for the ^{12}C and ^{40}Ca target nuclei, see ref.[10])

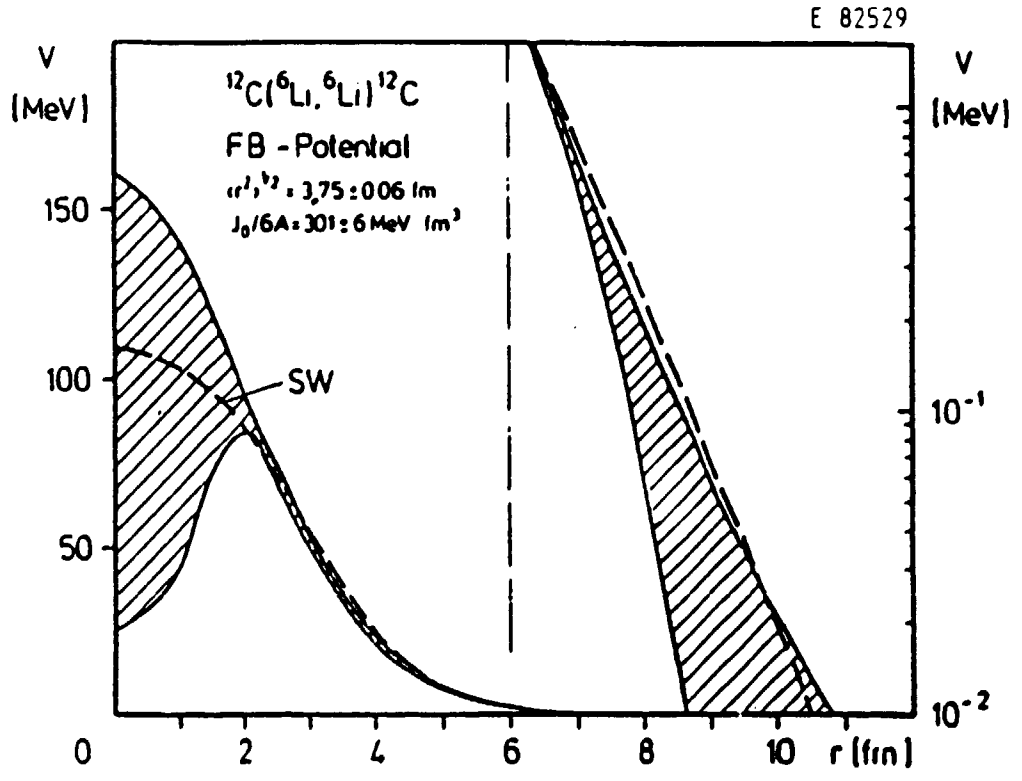

Fig. 11. Real part of the optical potential which reproduce the experimental angular distribution of ^{6}Li particle on ^{12}C target nucleus see fig. 10. Please notice that all potential curves inside the hatched area provide acceptable fits of the data, see ref.[10]).

The main problem for the next future years is to find orbiting or nuclear rainbow phenomena and to determine potential for combination of projectile and target mass more and more heavier. In this view the ^{6}Li experiment has produced beautiful data[10]. In fig. 10 are presented nuclear rainbow results induced by ^{6}Li heavy ions of 156 MeV incident energy. Nuclear rainbow is well evidenced for ^{12}C and ^{40}Ca target nuclei. The optical model analysis of J. Cook is very interesting since he was able for a given absorption to determine the region of sensitivity of the real potential, see fig. 11. All the smooth potential curves which belong to the hatched area produce acceptable fits of the ^{6}Li scattering data. We can conclude that the potential is well defined between 2.2 and 7 fm for a ^{12}C mean square radius of 3.75 fm. This result is pretty obvious : at small distance the inner partial waves are totally absorbed, break-up or fusion processes appear and do not contribute to the elastic cross

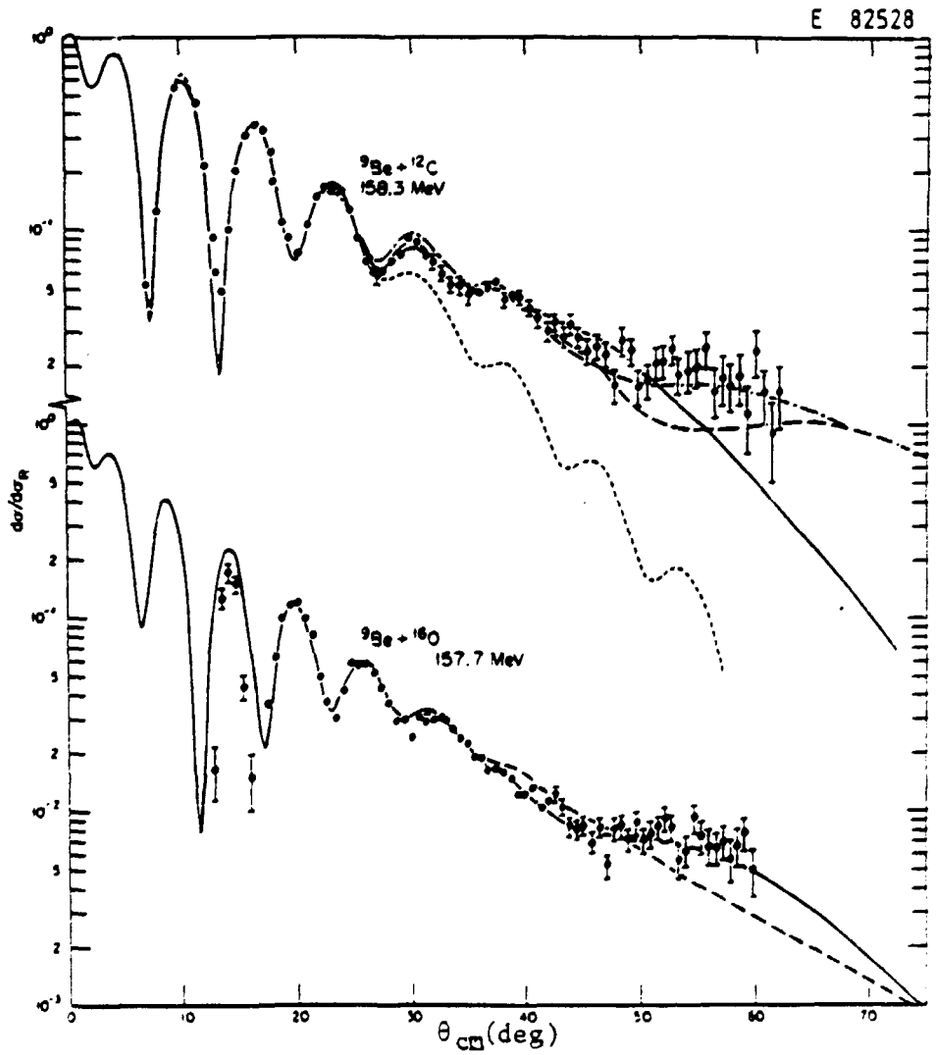

Fig. 12. Angular distributions of the ^{9}Be particle elastic scattering on ^{12}C on ^{16}O target nuclei. The curves are optical optical model fits, see ref.[11]).

section ; at large distance the nuclear potential is negligible in front of the long range unadjustable Coulomb potential.

Very recent studies have been pursed with ^{9}Be elastic scattering on ^{12}C and ^{16}O target nuclei[11]). Nuclear rainbow has been clearly evidenced, see fig. 12, and optical model potentials are pinned down.

5. RESONANCE PHENOMENA

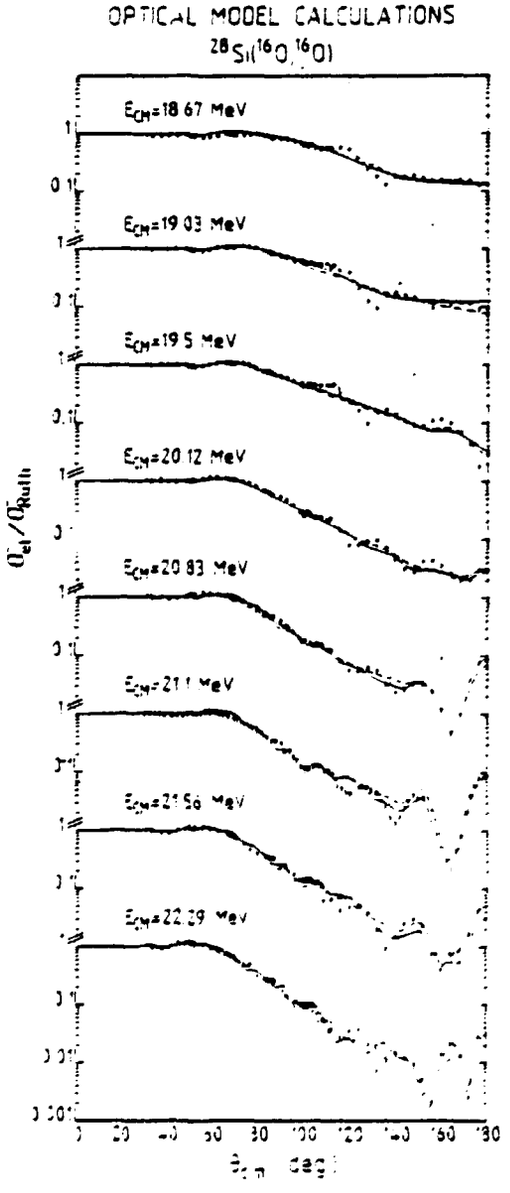

Fig. 13. Eight elastic scattering angular distributions of ^{16}O and ^{28}Si system measured just above the Coulomb barrier region of the first wide quasi-molecular resonant structure, see ref.[15]).

Heavy ion scattering for combination of targets and projectiles which belong to the 1p or 2s-1d shell has shown resonances and some of them are of the quasi molecular type[12-14]). These resonance phenomena are related in some way to orbiting phenomena and, in a cavalier manner, we can say that the orbiting phenomenon is the door-way state of the quasi-molecular structure. Such a coupling produces a considerable distortion of the observed elastic scattering angular distribution in the resonance region making pure optical model analysis questionable. It had turned out sometime that the fitting potentials own anomalous characters physically unrealistic. The quality of the fit is improved by adding, on the nuclear surface, perturbations which are not theoretically justified. An example of such an analysis is presented in fig.13 for the ^{28}Si, ^{16}O elastic scattering reaction measured just above the Coulomb barrier[15]). In the 180° c.m. excitation function, the top of the resonance is located at 21.1 MeV center of mass energy and the minimum at 19.5 MeV in the low energy side. The angular distributions have been fitted with the automatic search code

ECIS 73 of J. Raynal. The solid curves correspond for the real part to a Wood-Saxon potential with two Wood-Saxon derivative forms as surface perturbation terms. The imaginary part is of a Wood-Saxon type but with a large surface transparency up to the turning point of the grazing wave : small radius and very small diffusivity parametrize this imaginary part. The dashed curves are little worse fits but are obtained with the usual Wood-Saxon form for the real and imaginary part, of course large surface transparencies are also present. The corresponding S-matrix elements and total deflection function are given in fig. 14 for the maximum and first minimum of this quasi-molecular structure. For the angular distribution on the top of the resonance at 33.16 MeV ^{16}O incident energy (21 MeV c.m.), the deflection function and S-matrix are very irregular in the grazing wave region. That is not so much the case for the first minimum at 30.64 MeV incident energy (19.5 MeV c.m.). In the angular distribution, fig. 13, the potentials which best fit the data change at each energy, we can then conclude that we are dealing with a process more sophisticated than a pure orbiting phenomenon as it was for alpha particle scattering at several energies and on several target nuclei in the Zr region where the data are perfectly best fitted by a unique very simple potential.

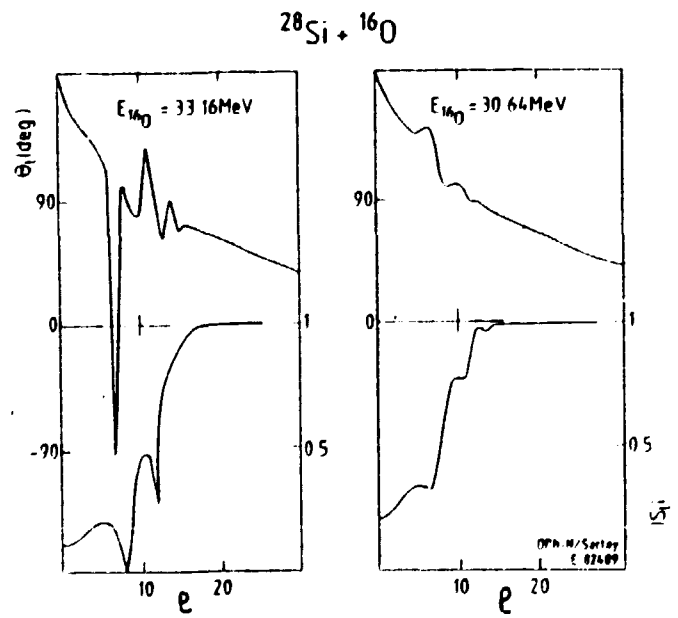

Fig. 14. Modulus of the optical model scattering matrix S along with the total optical model deflection function of the ^{28}Si and ^{16}O systems.

For the simple Wood-Saxon potential of $^{28}Si,^{16}O$ elastic scattering reaction, far-side and near-side splitting of the cross section has been performed. As it can be viewed on fig. 15 the near-side amplitude dominates

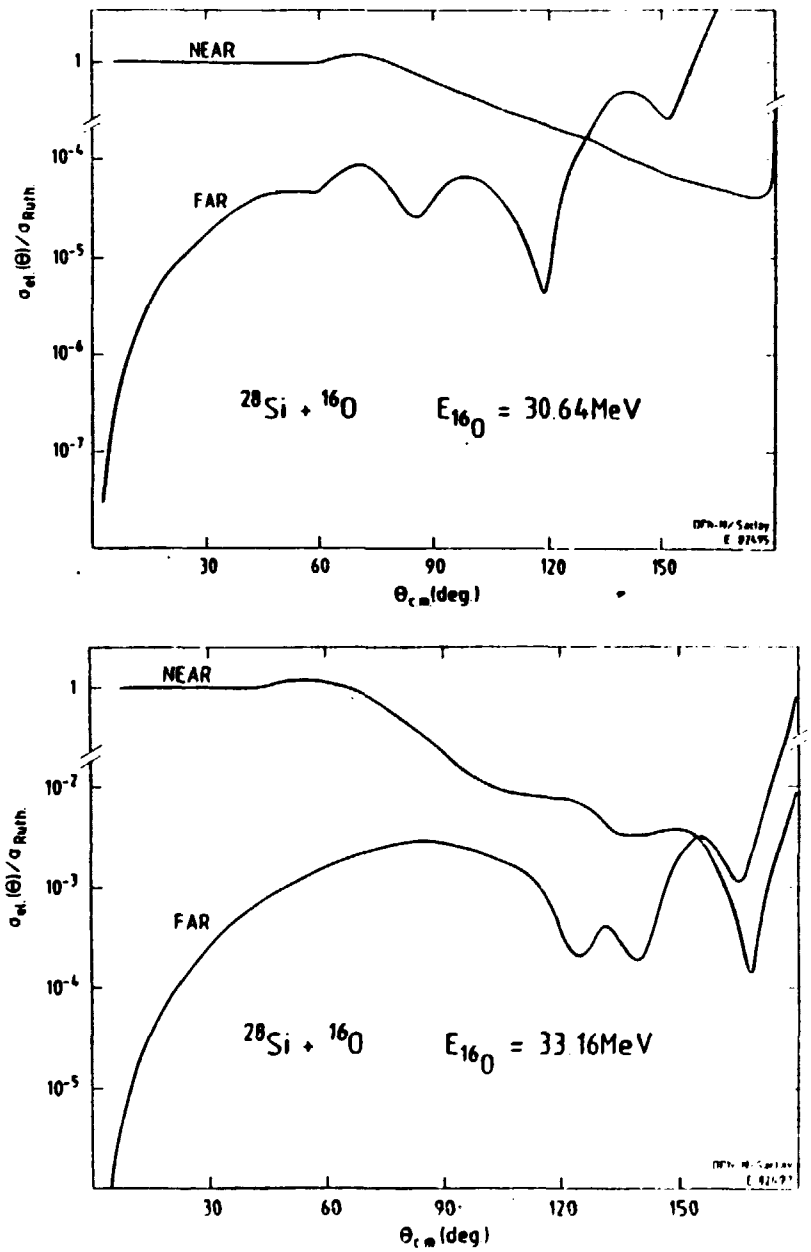

Fig. 15. The far-side and near-side decomposition of the elastic angular distribution top and low energy side minimum of the quasi-molecular resonance located at 21.1 MeV center of mass energy.

at forward angles and display a Fresnel pattern. On the other hand at backward angles the two components are of the same order of magnitude and produce an oscillatory pattern in the total cross section. Let us remark that out of resonance at 30.64 MeV ^{16}O incident energy (19.5 MeV c.m.) there is no more oscillation in the near contribution cross section at backward angles.

All the angular distributions of fig. 13 have been also analysed in term of the Frahn-Venter model including one Regge-pole parametrization. It is, first of all, very important to remark that the so-called Frahn Venter model[16]) is in fact an analytical best fit of the S- optical model

matrix elements generated by solving the Schrödinger equation for a diffractive and refractive potential : $W \neq 0$ and $V \neq 0$. This is the reason why this model is widely successful for elastic scattering of particles of mass greater than or equal to 4 amu.

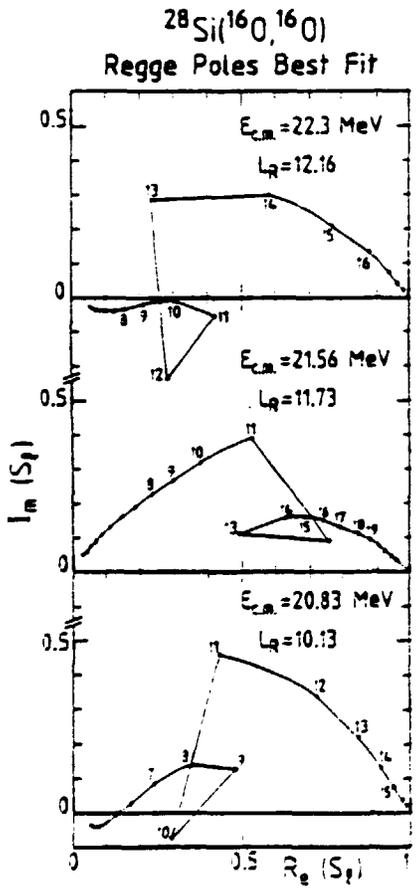

Fig. 16. Argand-Cauchy plot of the S-matrix element including the one Regge pole parametrization. The resulting calculated angular distributions are displayed on fig. 17.

In fig. 16 is presented, for three angular distributions, an Argand-Cauchy plot of the S-matrix which generates the corresponding angular distributions of fig. 17. The Regge pole produces a loop around the grazing wave in this S-matrix plot. The experimental angular distributions of fig. 17 are extremely well reproduced by the Regge pole analysis performed with the automatic search code FVRP, [ref.[17])]. The dashed curves are the background angular distributions produced by the Frahn-Venter parametrization alone.

It had been shown by T. Tamura et al.[18]) that Regge poles can be present in the S-matrix belonging to the optical model analysis. Shallow potential produces only one pole while deeper potentials possess several poles in the Argand-Cauchy representation. It had turned out at low incident energy that a single Regge pole is plenty enough to reproduce accurately the data. The forward angles of elastic scattering angular dis-

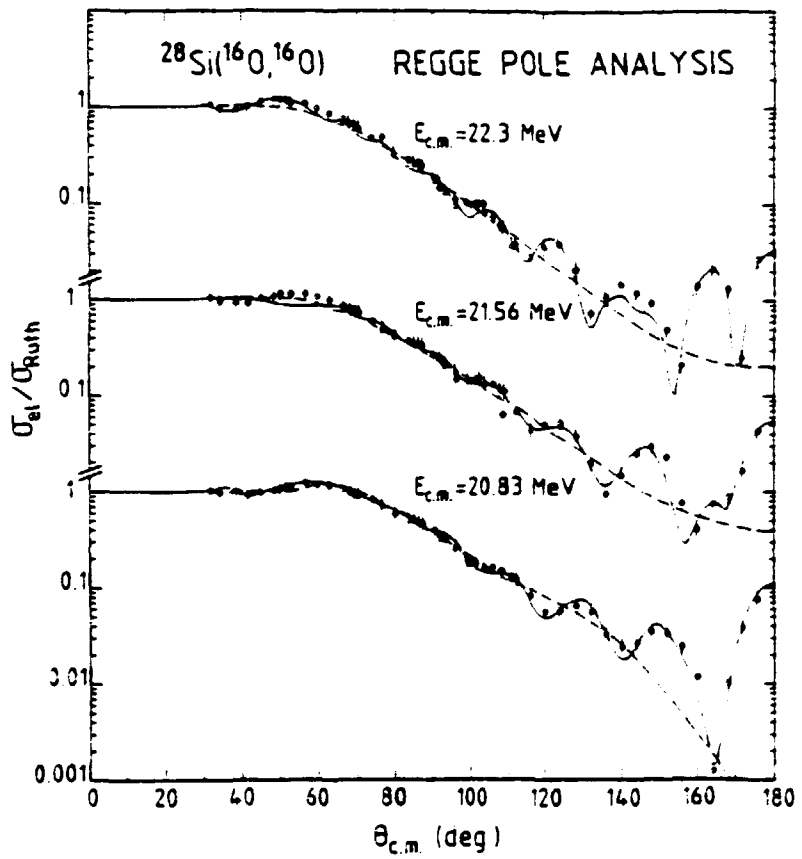

Fig. 17. Typical Regge pole analysis of the ^{28}Si and ^{16}O elastic scattering system, see text and fig. 16

tributions are reproduced by the background term, for instance Frahn Venter parametrization while the backward angle angular distributions are very sensitive to the Regge pole parameters. It had also turned out that the Regge pole parameters change indeed very rapidly with the variation of incident energy making the resonance phenomena extremely complex. Phase shift analysis is probably possible only at low incident energy where only few partial waves contribute to the elastic scattering cross sections. It is the mixture of two different mechanisms *orbiting* and *resonances* which made unsatisfactory all these analyses. Bumps in the elastic scattering excitation function can be due to several overlapping resonances ; statistical fluctuations of the scattering matrix elements have also been evidenced at higher center-of-mass energy[13,19].

6. CONCLUSION

Resonance phenomena on 4N nuclei systems are very difficult to disentangle from orbiting phenomenon described by pure optical model analysis. Orbiting phenomenon becomes very clear for heavy targets as well as

nuclear rainbow phenomenon at high incident energy. The disappearance of resonant effects in these two latter cases can be attributed to the large level density increase in the composite system and thus to the strong overlapping of many resonances.

Orbiting and nuclear rainbow allow a better description of the interior of the optical potential near the nuclear surface. Such studies have to be pursued for heavier and heavier mass combinations of target and projectile in order to probe better the nuclear potential in the surface region.

ACKNOWLEDGEMENTS

It is a pleasure to thank Dr. N. Alamanos[20]) for pointing out to us the possible use of the fortran code POISON of E. Plagnol for the R.C. Fuller decomposition of the elastic scattering in far-side and near-side components.

REFERENCES

1) Classical and quantum aspects of heavy ion collisions, Lecture Notes in Physics, Ed. H.L. Harney, P. Braun-Munzinger and C.K. Gelbke, Springer-Verlag (1975).
2) R.C. Fuller, Phys. Rev. C12 (1975) 1561 ; M.S. Hussein and K.W. McVoy, preprint MAD/NT/103 (1983) ;
K.W. McVoy and G.R. Satchler, submitted to Nucl. Phys. A (1983) ;
R. da Silveira and Ch. Leclerc-Willain, preprint IPNO/TH. 83-36 and IPNO/TH. 83-61 (1983).
3) K.W. Ford and J.A. Wheeler, Ann. Phys. (N.Y.) 7 (1959) 259.
4) W.H. Miller, J. Chem.,Phys. 51 (1969) 3631.
5) G. Igo and R.M. Thaler, Phys. Rev. 106 (1957) 126.
6) G.R. Satchler, Proceedingsof the International Conference on Reaction between Complex Nuclei, Nashville, F.K. Gowan, J.B. Ball and J.H. Hamilton ; North Holland Amsterdam/American Elsevier, N.Y., (1974), vol. 2, p. 1971.
7) M.E. Cobern, N. Lisbona and M.C. Mermaz, Phys. Rev. C13 (1976) 674 ; M.A.Q. Fernandes, B.T. Kim, N. Lisbona and M.C. Mermaz, Nucl. Phys. A317 (1979) 511.
8) M. Wit, J. Schiele, K.A. Eberhard, J.P. Schiffer, Phys. Rev. C12 (1975) 1447.
9) D. A. Golberg, Phys. Lett. 55B (1975) 59.

10) J. Cook, H.J. Gils, H. Rebel, Z. Majka and H. Klewe-Nebenius, Nucl. Phys. A388 (1982) 173 ;
J. Cook, ibidem, page 153.
11) G.R. Satchler, C.B. Fulmer, R.L. Auble, J.B. Ball, F.E. Bertrand, K.A. Erb and D.C. Hensley, Phys. Lett. 128B (1983) 147.
12) Resonances in Heavy Ion Reactions Proceedings, Bad Honnef, Germany 1981, Lecture Notes in Physics 156, edited by K.A. Eberhard (1982) Springer Verlag, Berlin, Heidelberg, New York.
13) D.A. Bromley, Proceedings of the International Conference on Reaction between Complex Nuclei, Nashville ; F.K. Gowan, J.B. Ball and J.H. Hamilton, North Holland Amsterdam/American Elsevier, New York (1974) vol. 2, p. 603.
14) P. Braun-Munzinger and J. Barrette, Physics Reports 87 (1982) 209.
15) M.C. Mermaz, E.P. Chavez-Lomeli, J. Barrette, B. Berthier and A. Greiner, Phys. Rev. C (1984) to be published.
16) W.E. Frahn and R.H. Venter, Ann of Phys. (N.Y.) 24, 243 (1963) and Nucl. Phys. 59 (1964) 651.
17) M.C. Mermaz, CEN of Saclay, unpublished.
18) T. Tamura and H.H. Wolter, Phys. Rev. C6 (1972) 1976 ;
T. Takemasa and T. Tamura, Phys. Rev. C18 (1978) 1282.
19) M.C. Mermaz, Phys Rev. C23 (1981) 755 ;
M.C. Mermaz, A. Greiner, B.T. Kim, M.J. LeVine, E. Müller and M. Ruscev, Phys. Rev. C24 (1981) 1512 ;
M.C. Mermaz, A. Greiner, M.J. LeVine, F. Jundt, J.P. Coffin and A. Adoun, Phys. Rev.C25 (1982) 2815.
20) N. Alamanos, Thesis, Paris University ;
N. Alamanos, M. Lamehi-Rachti, C. Levi, L. Papineau and P. Talon, Nucl. Phys. A363 (1981) 477.

APPENDIX A

The approximated forms of the function $\tilde{Q}_\ell^{\pm}(\theta)$ allow to identify them with negative and positive deflection angle, far and near trajectories respectively[2]).

$$\tilde{Q}_\ell^{\pm}(\cos\theta) = \left[2\pi(\ell + \tfrac{1}{2})\sin\theta\right]^{-1/2} \exp\left[\pm(\ell + \tfrac{1}{2})\theta - \frac{\pi}{4}\right]$$

Let us notice that the sign + corresponds to a negative deflection angle : for the trajectory and vice versa. The validity region of this relationship is :

$$\frac{1}{\ell} < \theta < \pi - \frac{1}{\ell} .$$

The accurate identity is in fact :

$$\tilde{Q}_\ell^{\pm}(\cos\theta) = \frac{1}{2}\left[P_\ell(\cos\theta) \mp i\,\frac{2}{\pi}\,Q_\ell(\cos\theta)\right]$$

The recurrence formula for either P_ℓ or Q_ℓ is with $z = \cos\theta$:

$$(\ell+1)W_{\ell+1}(z) - (2\ell+1)zW_\ell(z) + \ell W_{\ell-1}(z) = 0$$

where W stands either for P_ℓ or Q_ℓ.

We have for the first two polynomials :

a) $P_0 = 1$ and $P_1 = z$; $\qquad -1 \leq z \leq +1$

b) $Q_0 = \frac{1}{2}\,\mathrm{Log}\,\frac{1+z}{1-z}$ and $Q_1 = zQ_0 - 1$; $\qquad -1 \leq z < 1$